Metal-induced conformational changes in ZneB suggest an active role of membrane fusion proteins in efflux resistance systems

Fabien De Angelis[a,1], John K. Lee[b,1], Joseph D. O'Connell III[b], Larry J. W. Miercke[b], Koen H. Verschueren[c], Vasundara Srinivasan[c], Cédric Bauvois[d], Cédric Govaerts[a], Rebecca A. Robbins[b], Jean-Marie Ruysschaert[a], Robert M. Stroud[b,2], and Guy Vandenbussche[a,2]

[a]Centre de Biologie Structurale et de Bioinformatique, Laboratoire de Structure et Fonction des Membranes Biologiques, Faculté des Sciences, Université Libre de Bruxelles, CP 206/2, B-1050 Brussels, Belgium; [b]Department of Biochemistry and Biophysics, University of California, San Francisco, CA 94158-2517; [c]Laboratorium voor Ultrastructuur, Vlaams Interuniversitair Instituut voor Biotechnologie, Vrije Universiteit Brussel, B-1050 Brussels, Belgium; and [d]Institut de Recherches Microbiologiques Jean-Marie Wiame (IRMW), B-1070 Brussels, Belgium

Contributed by Robert M. Stroud, April 29, 2010 (sent for review February 4, 2010)

Resistance nodulation cell division (RND)-based efflux complexes mediate multidrug and heavy-metal resistance in many Gram-negative bacteria. Efflux of toxic compounds is driven by membrane proton/substrate antiporters (RND protein) in the plasma membrane, linked by a membrane fusion protein (MFP) to an outer-membrane protein. The three-component complex forms an efflux system that spans the entire cell envelope. The MFP is required for the assembly of this complex and is proposed to play an important active role in substrate efflux. To better understand the role of MFPs in RND-driven efflux systems, we chose ZneB, the MFP component of the ZneCAB heavy-metal efflux system from *Cupriavidus metallidurans* CH34. ZneB is shown to be highly specific for Zn^{2+} alone. The crystal structure of ZneB to 2.8 Å resolution defines the basis for metal ion binding in the coordination site at a flexible interface between the β-barrel and membrane proximal domains. The conformational differences observed between the crystal structures of metal-bound and apo forms are monitored in solution by spectroscopy and chromatography. The structural rearrangements between the two states suggest an active role in substrate efflux through metal binding and release.

Cupriavidus metallidurans CH34 | heavy-metal resistance | resistance nodulation cell division | periplasmic adaptor protein

Microorganisms depend on protective mechanisms to survive the effects of toxic compounds in the environment. In Gram-negative bacteria, resistance nodulation cell division (RND) - driven efflux systems confer resistance to many drugs and heavy metals (1, 2). The canonical RND-based system is formed by the association of three components: one integral to the plasma membrane, one integral to the outer membrane, and a periplasmic connector. The plasma membrane protein (RND) is a substrate/proton antiporter. The outer-membrane factor (OMF) spans a large part of the periplasm and provides the exit portal. The periplasmic membrane fusion protein (MFP) links these two components together. Based on the nature of their substrate, tripartite RND-driven efflux systems are divided into two subclasses: the hydrophobe/amphiphile efflux (HAE) and the heavy-metal efflux (HME) subclasses. The selectivity and function of many HAE-RND systems such as the Acr and Mex families have been determined, alongside crystal structures of the RND, OMF, and MFP components of various systems (3–13). However, knowledge of HME-RND systems, including substrate specificity and the basis for selectivity, is much more limited.

The integral plasma membrane components of the RND-based efflux systems are thought of as the pump; however, the discovery of increasing functions of MFPs shows that these proteins also play a major role in substrate transport. Several MFPs bind their respective substrates (14–16), facilitate substrate transport (17, 18), and are essential for transport in vitro (17). MFPs are also involved in OMF recruitment (19), and are also found in Gram-positive bacteria, where no OMF is present (20). Based on these and other observations, several hypotheses about the catalytic functions of MFPs have been proposed. These possible functions include: recognizing, binding, and shuttling of the substrate from the periplasm to the transporter; promoting access of the substrate to the transporter; promoting the open state of the OMF; and affecting the rate of turnover by having different affinities to transition states of the transporter (11, 12, 19, 21). The growing body of evidence establishes MFPs as essential components of the efflux function of RND-driven complexes.

To examine the specificity and possible role of substrate binding and transport in an MFP, we address the metal binding specificity and the crystal structure of ZneB, the MFP from *Cupriavidus metallidurans* CH34, at 2.8 Å resolution. ZneB belongs to the ZneCAB HME-RND system found in *C. metallidurans* CH34, a Gram-negative bacterium specialized to survive in soil polluted with high concentrations of heavy metals. Twelve potential HME-RND systems have been identified in the *C. metallidurans* CH34 genome. The numerous RND transporters is exceptional and indicates high-level resistance to heavy metals; however, the literature provides limited experimental data regarding but a few of them (22). Here we show zinc as the specific ligand for ZneB, derive the distinct characteristics of an HME-type MFP, and propose a mechanism of zinc binding and transport suggested by the structure.

Results

Heavy-Metal Binding Properties of ZneB. With little known about the preferential substrates of Zne, we characterized the metal binding selectivity of ZneB toward Zn^{2+}, Cd^{2+}, Co^{2+}, Mn^{2+}, Ni^{2+}, Pb^{2+}, Cu^{2+}, Cu^{+}, and Ag^{+}. With the exception of manganese, these ions have been identified as potential substrates for HME-RND systems (22). After incubation of purified protein with four molar equivalents of the metal ions, samples were analyzed by mass spectrometry (MS) under nondenaturing conditions to preserve the potential protein-ion complexes (23). Recombinant

Author contributions: F.D.A., J.-M.R., and G.V. designed research; F.D.A., J.K.L., J.D.O., L.J.W.M., K.H.V., V.S., C.B., C.G., R.A.R., and G.V. performed research; F.D.A., J.K.L., and G.V. analyzed data; and F.D.A., J.K.L., R.M.S., and G.V. wrote the paper.

The authors declare no conflict of interest.

Freely available online through the PNAS open access option.

Data deposition: Atomic coordinates and structure factors for ZneB structures have been deposited in the Protein Data Bank, www.pdb.org (PDB ID code 3LNN).

[1]F.D.A. and J.K.L. contributed equally to this work.

[2]To whom correspondence may be addressed. E-mail: stroud@msg.ucsf.edu or vbussche@ulb.ac.be.

This article contains supporting information online at www.pnas.org/lookup/suppl/doi:10.1073/pnas.1003908107/-/DCSupplemental.

ZneB has an experimental molecular mass of 38,749 Da (Fig. 1), identical to the theoretical molecular mass of 38,749.12 Da. After addition of zinc (standard atomic mass 65.38 Da), the mass of the major peak increased to 38,814 Da, implying specific binding of one Zn^{2+} to the protein. ZneB incubated with Cd^{2+}, Co^{2+}, Mn^{2+}, or Ni^{2+} resulted in no mass shift, indicating no interaction between these ions and ZneB (Fig. S1). In the Pb^{2+}-treated sample, a very minor peak appeared at 38,956 Da, corresponding to nonspecific binding of one Pb^{2+}. Mass spectra recorded after addition of Cu^{2+}, Cu^{+}, or Ag^{+} gave mixed stoichiometries, suggesting nonspecific binding of these metal ions to the protein.

The dissociation constant (K_D) for the Zn-ZneB complex was determined by direct binding assayed by electrospray ionization (ESI) MS. This technique has been used to quantify noncovalent protein-ligand interactions (25), and has been shown to accurately reflect protein-ligand binding characteristics in solution (26, 27). After titration of ZneB with zinc, the K_D was determined to be ~3–4 μM using the model described by Mathur et al. (28). Thus, ZneB specifically binds zinc ions only of those tested here, with 1:1 stoichiometry. We propose that the Zne system is involved in the efflux of a narrow range of substrates and more specifically of zinc ions.

Effect of Zn^{2+} Binding on Structure: Zn-ZneB Versus Apo-ZneB. Both native and selenomethionine ZneB crystallized in the presence of two molar equivalents of Zn^{2+} in space group $I4_122$ with two molecules (A and B, representing the zinc-bound and the apo forms, respectively) in the asymmetric unit. Phases were determined by the single-wavelength anomalous dispersion (SAD) method using data to 3.3 Å resolution. A native dataset to 2.8 Å was used for refinement (Table S1). Residues 11–349 out of 349 in A and residues 39–293 in B were interpreted in the structure and refined.

ZneB has the same overall organization as the MFP from the monovalent-ion-transporting CusB (HME-MFP from *Escherichia coli*) (13) and the amphiphile-selective MexA (HAE-MFP from *Pseudomonas aeruginosa*) (11). The fold consists of four distinct domains consisting of a membrane proximal (MP) domain, a β-barrel domain, a lipoyl domain, and an α-helical hairpin domain (Fig. 2). The polypeptide chain begins in the MP domain and moves on through the β-barrel and lipoyl domains out to the helical hairpin, where it reverses back forming additional components of each domain, returning to the MP domain.

The electron density map shows one Zn^{2+} in A coordinated between the MP and β-barrel domains (Fig. 2). No Zn^{2+} is bound in B and the MP domain in B is not visible, presumably due to flexibility of the ensuing linker and the absence of Zn^{2+}. The MP domain was also not visible in the early structures of MFPs such as MexA (9, 10) and MacA (29). The flexibility of the MP domain has been proposed to be a key element in the substrate binding and release mechanisms of MFPs (11, 21). In addition, the

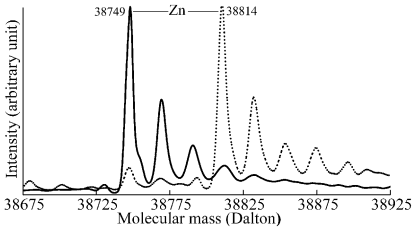

Fig. 1. Mass spectra of apo-ZneB (solid line) and of ZneB incubated with four molar equivalents of Zn^{2+} (dashed line). Intensities were normalized. The molecular mass of 38,749 Da corresponds to the recombinant protein with unprocessed N-terminal methionine due to the presence of a lysine in position P1′ inhibiting the methionine aminopeptidase activity (24). Secondary peaks at higher molecular masses correspond to sodium adducts.

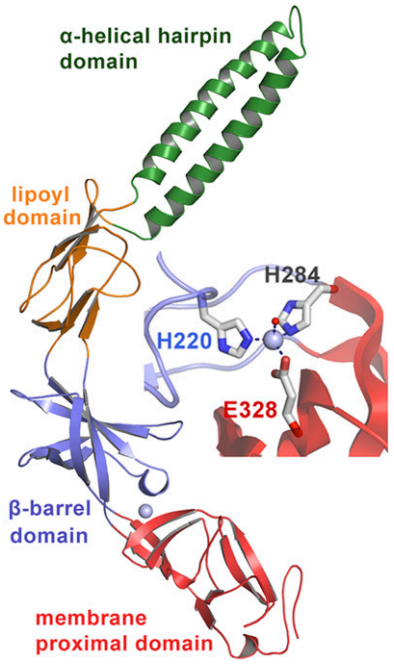

Fig. 2. The crystal structure of zinc-bound ZneB (molecule A). The structure follows the four-domain architecture characteristic of MFPs, MP (red), β-barrel (blue), lipoyl (yellow), and hairpin (green). Zn^{2+} is represented as a blue sphere. The hairpin domain is a coiled-coil structure similar in length to that in MexA and AcrA. Inset: Zn^{2+} is coordinated by H220, H284, E328, and a water molecule.

domains in B are arranged in a more extended fashion, whereas in molecule A they adopt a crescent shape (Fig. 3).

Zn^{2+} is tetrahedrally coordinated between the Nε of H220 (from the β-barrel domain), E328 (from the MP domain), the Nε of H284 (from the linker connecting those two domains), and a water molecule. This Zn^{2+} coordination is similar to that seen before in the structure of the zinc transporter CzrB (30). Thus, the β-barrel and MP domains cooperate in binding Zn^{2+} as the two domains adopt a specific arrangement. The affinity of ZneB for Zn^{2+} was initially suggested from the necessary presence of the metal for crystal growth and later validated by its presence and coordination in the structure of A, but interestingly not B.

Mutations Validate the Zn Binding Site. Mutation of each of the Zn^{2+} residues to serine H220S, H284S, and E328S abolished Zn^{2+} binding as measured by mass spectrometry (as above), whereas mutation of a fourth residue (E285) located near the coordination site and used as a control did not (Fig. S2). Infrared spectroscopy was used to assess the conformational integrity of the mutant proteins. The characteristic amide I and amide II bands arise from different vibrations of the peptide bond with shapes that are sensitive to the conformation of the protein (31). Comparison of the four mutant spectra with that of ZneB does not reveal any mutation-induced structural differences (Fig. S3).

Comparison of ZneB, CusB, and MexA. The structure of Zn^{2+} transporting ZneB was compared with CusB in the HME subfamily (13) and to MexA in the HAE subfamily (11). Whereas the general four-domain structure is shared by all, the fold of each domain is most similar to the monovalent-cation (Cu^{+} and Ag^{+}) -transporting CusB, with some divergence from the amphiphile transporter MexA, especially in the MP domain. MexAB-OprM pumps out many amphiphiles, including antibiotics, organic dyes, detergents, and organic solvents. The root-mean-square deviation

Fig. 3. Superimposition of molecules A (orange) and B (slate), showing that ZneB bends and adopts a closed, crescent shape upon zinc binding, whereas apo-ZneB adopts a more linear shape. The MP domain of B is unresolved and probably extends the protein in the direction of the linker to the β-barrel domain.

Fig. 4. Overlay of β-barrel (*Upper*) and MP (*Lower*) domains of ZneB (orange), CusB (yellow), and MexA (blue). Rmsd values (Cα) are as follows: β-barrel domains, ZneB/CusB = 1.82 Å and ZneB/MexA = 3.40 Å; MP domains, ZneB/CusB = 1.40 Å and ZneB/MexA = 8.57 Å.

(rmsd) (Cα) between the MP domains of ZneB and those of CusB and MexA is 1.40 and 8.57 Å, respectively (Fig. 4).

MP and the β-barrel domains are involved in substrate binding in ZneB and CusB—the only cases where substrate binding is seen in crystal structures of MFPs. However, differences must accommodate the different chemical properties and coordination geometries between transition metal ions and hydrophobic/amphiphilic molecules in HMEs and in HAEs, respectively (Fig. 4). The MP domain may be the central core of MFPs' activity through specific substrate binding and release to the RND. Folding of the β-barrel domains of ZneB, MexA, and CusB is very similar, except in the region facing the MP domains, especially between ZneB and MexA (Fig. 4). Overall, the rmsd (Cα) of this domain between ZneB versus CusB and MexA is 1.82 and 3.40 Å, respectively. The main difference lies in the length of the helix in the β-barrel domain that faces the MP domain. This difference is probably related to selectivity rather than to a simple structural variation, because one of the residues involved in the Zn^{2+} binding motif of ZneB is located in this region.

To analyze this difference in substrate binding between the two members of the HME-MFPs, CusB and ZneB, we analyzed the structural and sequence differences between them. The structures of CusB and ZneB reveal distinctly different modes and locations of metal binding. We aligned and analyzed the sequences of several HME-MFPs (Fig. S4) and built a similarity tree (Fig. S5). The dendrogram shows two distinct clusters named CzcB-like proteins (assumed to be involved in divalent metal cation efflux) and CusB-like proteins (assumed to be involved in monovalent metal cation efflux). ZneB belongs to the CzcB-like cluster. Sequence alignment of the CusB-like proteins shows that the metal binding residues of the CusB MP domain, as seen in the crystal structure (13), are not conserved (Fig. S4). Conversely, three methionine residues of CusB (M21, M36, and M38) that have been identified as essential for Ag^+ binding, as well as for Cu^+ resistance of the cell in vivo (14), are highly conserved throughout all CusB-like proteins. None of the residues involved in Cu^+ and/or Ag^+ binding in CusB are conserved in ZneB, and we found no specific binding of either ion by ZneB. Two of the residues involved in the Zn^{2+} binding site of ZneB, H220 and H284, are not conserved among HME-MFPs (although they are loosely conserved in HmvB and ZniB from *C. metallidurans* CH34), whereas the third residue, E328, is highly conserved, especially among CzcB-like MFPs.

Structural Flexibility and Rearrangement. Structures of the Zn^{2+}-bound and apo-ZneB, molecules A and B, seen in the same crystal unit cell, suggest a conformational change upon Zn^{2+} binding. The majority of the MP domain of B is disordered, but the linker strand between the β-barrel and the MP domain suggests that the location of the latter is dramatically different from the Zn-bound form. To assess the degree of structure change in solution and separate the contributions due to crystal packing, we evaluated the changes in apparent size and shape by size-exclusion chromatography (SEC), infrared spectroscopy, and tryptophan quenching fluorescence assay.

Analytical SEC retention volumes depend on the shape of the protein. ZneB (~39 kDa) is decidedly elongated in shape. Therefore, it is expected to run at the position of a globular protein of higher apparent molecular volume on SEC. Zn-ZneB elutes from the column at a retention volume of 14.5 mL, corresponding in position to that of a globular protein of 44 kDa (Fig. 5). The unbound form elutes at a retention volume of 13.9 mL, corresponding to a globular protein of 61 kDa. This shows that ZneB undergoes a conformational change upon Zn^{2+} binding to a more compact state as in A, versus the linear arrangement of domains in B. Moreover, SEC shows that ZneB is a monomer in solution, like every other MFP (14, 21, 29), and that zinc binding has no influence on its quaternary structure. Similar results have been obtained for CusB from *E. coli* (14).

The structures of apo- and Zn^{2+}-ZneB were compared using infrared spectroscopy. The spectra are very similar, but not

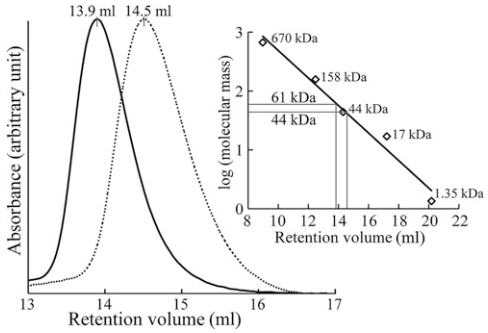

Fig. 5. Analytical SEC performed on a Superdex 200 column of apo- and Zn^{2+}-ZneB (protein:zinc molar ratio 1:2). Apo-ZneB (solid line) elutes at 13.9 mL, whereas Zn^{2+}-ZneB (dashed line) elutes at 14.5 mL. Absorbance values were normalized. Inset plot shows the retention volumes of globular proteins used as standards.

identical (Fig. 6). A difference spectrum was obtained by subtracting the spectrum of the apo form from the spectrum of the metal-bound form (Fig. 6, inset). In the difference spectrum, the positive and negative deviations are consequently associated with structural modifications of ZneB upon zinc binding. A major positive peak appearing at 1,635 cm^{-1} with a shoulder at 1,686 cm^{-1} can be assigned to an increase in the β-sheet content (31). Because the β-sheet content is equivalent in visible parts of molecules A and B, this structural gain might take place in the MP domain. Because residues involved in zinc coordination sites are often located on β-sheets (32), zinc binding might trigger the organization of residue E328 and its vicinity in β-sheets. A negative peak appears at 1,564 cm^{-1}. Because a glutamate side chain normally absorbs at 1,567 cm^{-1}, this negative peak might point to vibrational modification that the E328 side chain undergoes upon zinc binding. No attempt was made to assign the negative peak observed at 1,615 cm^{-1}. Thus, these spectral shifts are consistent with the differences between A and B.

Tryptophan accessibility was monitored in attempts to evaluate the change in solution conformation induced by Zn^{2+}. Upon addition of Zn^{2+}, tryptophan fluorescence was quenched more effectively by acrylamide, indicating overall higher accessibility of the two tryptophan residues, W191 located on the lipoyl domain and W310 located on the MP domain (Fig. 7 and Fig. S6). W191 occupies exactly the same conformation in both A and B, suggesting that its accessibility is not modified upon zinc addition. W310 lies in the MP domain, visible only in molecule A, thus preventing any comparison of W310 conformations using crystallographic data. Nevertheless, alteration of W310 quenching could reflect an internal structural rearrangement of the MP domain triggered by Zn^{2+} binding.

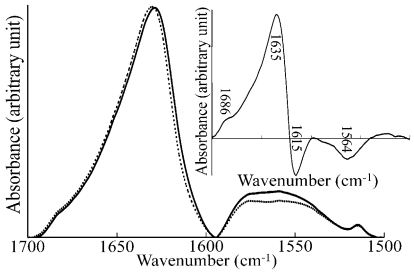

Fig. 6. Attenuated total reflection Fourier-transformed infrared (ATR-FTIR) spectra of deuterated apo-ZneB (solid line) and Zn-ZneB (dashed line). Plotted curves are averaged from three independent measurements. Absorbance values were normalized. Inset shows the difference spectrum obtained by subtracting the apo-ZneB from the Zn^{2+}-ZneB spectrum.

Discussion

ZneB substrate binding ability and structural differences between Zn^{2+}-bound (A) and apo (B) support the hypothesis of an active role of MFPs in RND-driven efflux. A docking model of MexA on the antiporter MexB localizes the MP domain near a pocket responsible for drug access and binding in the antiporter (11). Substrate carried by MexA was proposed to be released to the antiporter through MP domain localization and flexibility (11, 21). Likewise, structural modifications of ZneB might trigger substrate delivery to the antiporter (ZneA). ZneB bound to its antiporter will be coupled to the conformational changes of the pump in its "functional rotation cycle" (4, 5). Because the Zn^{2+} binding site of ZneB is composed of residues from two different domains of the protein and a third from the flexible linker between them, binding can be easily disrupted with a small shift in the location of the two domains. The evidence observed in the crystal structure of ZneB suggests a change in conformation would lead from the open apo form (termed the "unrotated" state in MexA), where the MP domain is located in the straight extension of the three other domains, to the closed (crescent-shaped) zinc-bound form (termed the "rotated" state in MexA) (Fig. 8).

The high conservation of E328 throughout HME-MFPs of different mono- and divalent-ion specificities implies that this residue might be involved in more diverse mechanisms than substrate binding alone. Other possible functions include interaction with the antiporter to facilitate substrate handoff and influence the turnover rate by modifying ZneB affinity for the transporter. ZneB binds specifically with an ~3 μM K_D for Zn^{2+}, compatible with subsequent cation release to the antiporter. The flexibility in the linker regions between the four domains is also consistent with differences observed in the location of each domain between the different MFP crystal structures. The structural rearrangement upon substrate binding of the MP domain might be an essential element underlying the hypothesis that MFP may have a role in energy-coupling between the antiporter and the OMF.

The substrate binding ability of ZneB, a periplasmic protein, indicates that the Zne efflux complex is likely to detoxify the cell from the periplasm. This system could therefore prevent damage done to the cell before heavy-metal ions cross the plasma membrane. This detoxification mechanism is possibly adopted by most of the HME-RND systems. These systems might also work in synergy with inner-membrane ATPase transporters or cation diffusion facilitators which expel ions from the cytoplasm to the periplasm (1, 33). However, the ability of RND-driven efflux systems to capture their substrate from the cytoplasm requires further investigation (34). Alternatively, MFPs might act as a regulator by substrate-induced MFP conformational changes, promoting substrate transport by the entire complex. Substrate release by the

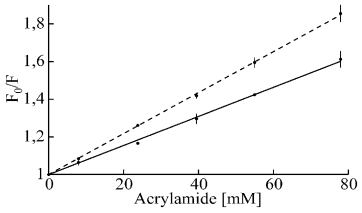

Fig. 7. Stern–Volmer plots of ZneB tryptophan quenching by acrylamide in the absence (solid line) and presence (dashed line) of two molar equivalents of Zn^{2+}. F is the measured fluorescence intensity and F_0 is the fluorescence intensity in the absence of acrylamide. Values are the mean ± SD (n = 3).

MICROBIOLOGY

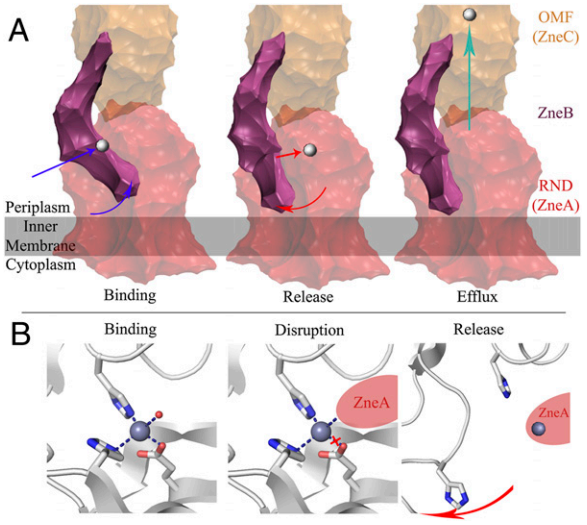

Fig. 8. Schematic representation of proposed ZneB structural cycling throughout RND-driven substrate efflux. (*A*) Large view of the three components. Protein shapes are based on surface rendering of ZneB (purple; molecules A for "binding" and B for "release" and "efflux"), AcrB (red), and TolC (orange) crystal structures. (*B*) Detailed close-up of the zinc binding/release process based on apo- and zinc-bound crystal structures of ZneB.

MFP back to the antiporter may not be necessary for the transport to function. When substrate periplasmic concentration drops below a certain threshold, equilibrium would favor the apo-MFP form, triggering repression of the transport activity. Thus, MFP could regulate the concentration dependence of efflux in a cooperative fashion, allowing for physiologic concentrations of the ions.

The exact up-regulation and functional necessity of the Zne system has yet to be defined, but the insights we have gathered from the structure and binding specificities of ZneB reveal a specialized detoxification machinery. The nonconserved zinc binding motif of ZneB and the remote clustering of this protein in the similarity tree (Fig. S5) reveal unique characteristics of ZneB not shared with other CzeB-like proteins. This is in agreement with the sharp selectivity of ZneB for Zn^{2+}, whereas all other known HME-RND systems target at least two or three cations.

Expressing an RND-driven efflux system to detoxify a single heavy metal with intermediate toxicity such as zinc is an energetically expensive strategy, and *C. metallidurans* also carries the Czc system, which is responsible for Zn^{2+} detoxification along with Cd^{2+} and Co^{2+}. Because *C. metallidurans* CH34 carries a large number of RND systems in its genome, with overlapping specificities, it is able to mount a multilayered response to a large range of metal-rich biotopes (22, 35).

Materials and Methods

Protein Expression and Purification. The coding sequence of ZneB(37–385) corresponding to the mature protein devoid of its signal peptide (Q1LCD7) was amplified by PCR with high-fidelity DNA polymerase (Fermentas) using genomic DNA from *C. metallidurans* CH34 as template. A 3C-protease cleavage site was introduced at the ZneB C terminus. PCR product was ligated into plasmid pET30b (Novagen) between NdeI and XhoI restriction sites, upstream of a His-tag-coding sequence. The construct was transformed into *E. coli* strain BL21(DE3) (Novagen) for expression, or into methionine auxotrophic strain B834(DE3) (Novagen) for selenomethionine-labeled protein expression. BL21 (DE3) cells were grown at 37 °C in Luria–Bertani medium to an OD_{600nm} of 0.8. Expression was induced by 0.5 mM isopropyl-β-D-1-thiogalactopyranoside (IPTG) for 3.5 h. B834(DE3) cells were grown at 37 °C in minimal medium containing methionine to an OD_{600nm} of 1. Cells were harvested, resuspended in minimal medium, and starved of methionine for 3 hr. Seleno-L-methionine was added as the sole methionine source. Expression was induced by 0.5 mM IPTG for 8 h. Cell pellets were resuspended with chilled purification buffer (20 mM Hepes, pH 8.0, 300 mM NaCl) containing 20 mM imidazole, DNase, and protease inhibitors (Complete; Roche). Cells were lysed in an EmulsiFlex (Avestin) at 4 °C. Cell debris was removed by centrifugation at 140,000 × g for 30 min at 4 °C. Supernatant was mixed with Ni-NTA resin (Qiagen). Resin was washed with chilled purification buffer containing 50 mM imidazole and protein was eluted with 250 mM imidazole. The protein sample was loaded onto a PD-10 desalting column (GE Healthcare) using storage buffer (20 mM Hepes, pH 7.5, 150 mM NaCl). The His tag was removed by overnight digestion in 3C-protease at 4 °C. Uncleaved His-tagged ZneB and 3C-protease (carrying a His tag) were removed using Ni-NTA resin. The sample was fractionated on a Superdex 200 SEC column. Fractions containing ZneB were pooled and protein was concentrated to a desired value (measured with Nanodrop; Thermo Scientific) using an Amicon filter device (30 kDa cutoff; Millipore). Protein purity and stability were assayed by SEC and SDS/PAGE. Protein integrity, His-tag cleavage, and selenomethionine replacement efficiencies were verified by MS.

Mass Spectrometry. Mass spectra were acquired on a Q-TOF Ultima API spectrometer (Waters/Micromass) equipped with a nanoelectrospray source and operating in positive-ion mode. Parameters used for binding experiments were set as follows: capillary voltage 1600 V, cone voltage 50 V, source block temperature 100 °C, and pirani pressure 2.2 mbar. ZneB was solubilized in 20 mM ammonium acetate (pH 6.9). Metal solutions were prepared using $ZnSO_4$, $CdCl_2$, $CoCl_2$, $NiCl_2$, $MnCl_2$, $CuCl_2$, $Pb(CH_3COO)_2$, and $AgNO_3$ salts. Cu^+ was obtained by adding ascorbate to Cu^{2+} solution. Zinc solution was prepared using an atomic absorption standard (Fluka). For the K_D determination, titration was conducted with constant protein concentration (4 μM) and varying zinc concentration (0–20 μM). Each titration experiment was realized in triplicate. Data acquisition was performed using a MassLynx 4.0 system (Waters/Micromass). Deconvoluted spectra were generated with MaxEnt1 (Waters/Micromass). After baseline subtraction, peak areas of apo and metallated forms (and their respective adducts) were determined using the MassLynx integration program. Due to the overlapping of the ion-bound form with some apo-ZneB adducts, the contribution of the latter was estimated for each spectrum and subtracted from the area of the Zn-bound form. For accurate molecular mass determination, protein was solubilized in 50% acetonitrile/1% formic acid (vol/vol) after desalting on $ZipTipC_{18}$ resin (Millipore). Molecular mass was determined after MaxEnt1 deconvolution of the mass/z raw data.

Crystallization and Data Collection. Crystals were grown by the hanging-drop vapor-diffusion technique. Four microliters of a 7 mg/mL ZneB solution added with 360 μM $ZnSO_4$ was mixed with 2 μL of a well solution containing 0.1 M Na-acetate (pH 5.4), 1.9 M Na-formate, and 3% ethanol. Crystals grew to full size within a few days at 20 °C (0.4 × 0.4 × 0.2 mm^3). When none of the ions Cd^{2+}, Co^{2+}, Ni^{2+}, or Cu^{2+} was added, ZneB did not crystallize. Crystals were cryoprotected in nylon loops (Hampton Research) using well solution containing 30% ethanol. A slight contaminant was present within crystals as revealed by SDS/PAGE. It was removed after incubation of purified ZneB with hydroxyapatite resin (Bio-Rad). This treatment increased the diffraction limit from 3.2 to 2.8 Å. Two microliters of 5.5 mg/mL selenomethionine-labeled ZneB solution containing 280 μM in $ZnSO_4$ was mixed with 2 μL of well solution containing 0.1 M Na-acetate (pH 4.8), 1.75 M Na-formate, and 10% glycerol. Crystals were cryoprotected using well solution containing 25% glycerol. Native datasets were collected at 100 K at beamline ID23-1 at the European Synchrotron Radiation Facility (ESRF, Grenoble, France). SAD datasets were collected at 100 K at beamline 8.3.1 at the Advanced Light Source (ALS, Berkeley, CA).

Structure Determination and Refinement. Data were indexed and scaled using HKL2000 (36). A random sampling (5%) of data was omitted from the structure factors during refinement for R_{free} calculations. Initial phase calculations and solvent flattening were done using the PHENIX system (37). Eight selenium sites were located and initial maps were calculated at 3.4 Å resolution. The initial model was then refined using the 2.8 Å data. The model was built using Coot (38) and refinement was using Refmac5 (39) and PHENIX. Figures were generated using PyMOL (40).

Mutagenesis. Residues H220, H284, E285, and E328 were individually substituted for serine by site-directed mutagenesis (Stratagene) using double-stranded plasmid (pET30b carrying the *zne*B gene) template and mutagenic primers. Mutations were confirmed by sequencing (GATC Biotech). Expression and purification of mutants were as for wild-type.

Size-Exclusion Chromatography. SEC was performed using a Superdex 200 10/300GL analytical column on an Äkta Purifier (GE Healthcare). The column was

preequilibrated with 50 mM Hepes (pH 7.5) and calibrated with SEC globular molecular mass standards (Bio-Rad) (thyroglobulin, 670 kDa; γ-globulin, 158 kDa; ovalbumin, 44 kDa; myoglobin, 17 kDa; vitamin B12, 1.35 kDa).

Infrared Spectroscopy. ZneB was solubilized in 2 mM Hepes buffer (pH 7.5). ATR-FTIR spectra were recorded at 20 °C on an Equinox 55 infrared spectrophotometer (Bruker Optics) equipped with a liquid nitrogen-cooled mercury-cadmium-telluride detector. The internal reflection element was a diamond crystal (2 × 2 mm) with an aperture angle of 45° yielding a single internal reflection. Protein was spread at the diamond crystal surface by evaporation of the sample under nitrogen flow. Two hundred fifty-six accumulations were performed to improve the signal/noise ratio. The spectrometer was continuously purged with dried air. Spectra were recorded at a nominal resolution of 2 cm^{-1}. Hydrogen was exchanged with deuterium by flushing D_2O-saturated nitrogen.

Fluorescence Spectroscopy. Tryptophan fluorescence quenching experiments were carried out with acrylamide quencher. ZneB in 20 mM Hepes (pH 7.5), 150 mM NaCl buffer was titrated with 3 M acrylamide. Fluorescence was monitored at 20 °C on an SLM Aminco 8000 fluorometer (Horiba) using excitation and emission wavelengths of 290 and 333 nm, respectively. Quenching data were analyzed according to the Stern–Volmer equation for collisional quenching: $F_0/F = 1 + K[Q]$, where F_0 and F are the fluorescence intensities in the absence and presence of quencher, respectively, [Q] is the molar concentration of quencher, and K is the Stern–Volmer quenching constant. Data were subjected to a linear fit.

Sequence Alignment. Sixty-four HME-MFP sequences were selected using UniProtKB. No BLAST was performed to avoid a biased sequence pool. Proteins were selected for their unequivocally belonging to the HME-MFP family to avoid any HAE-MFPs. When not specified in the UniProtKB entry, signal peptides were identified and removed using SignalP (41). Alignment of mature HME-MFP sequences was generated using Clustal X (42) using default parameters and iteration at each alignment step.

ACKNOWLEDGMENTS. We thank the staffs at beamlines BM30A, ID23-1 (ESRF), and 8.3.1 (ALS). We thank Max Mergeay for fruitful discussion and help in renaming ZneB, Pat Greene for editing the manuscript, and Erik Goormaghtigh for programming in Matlab. F.D.A. is a Research Fellow for the Fonds pour la Formation à la Recherche dans l'Industrie et dans l'Agriculture (Belgium). The use of the BM30A beamline was supported by the Fonds National de la Recherche Scientifique (Contract IISN 4.4505.00, Belgium). Support to R.M.S. for this work was provided by National Institutes of Health Grant 5U54GM074929.

1. Nies DH (2003) Efflux-mediated heavy metal resistance in prokaryotes. *FEMS Microbiol Rev* 27:313–339.
2. Nikaido H, Takatsuka Y (2009) Mechanisms of RND multidrug efflux pumps. *Biochim Biophys Acta* 1794:769–781.
3. Murakami S, Nakashima R, Yamashita E, Yamaguchi A (2002) Crystal structure of bacterial multidrug efflux transporter AcrB. *Nature* 419:587–593.
4. Murakami S, Nakashima R, Yamashita E, Matsumoto T, Yamaguchi A (2006) Crystal structures of a multidrug transporter reveal a functionally rotating mechanism. *Nature* 443:173–179.
5. Seeger MA, et al. (2006) Structural asymmetry of AcrB trimer suggests a peristaltic pump mechanism. *Science* 313:1295–1298.
6. Sennhauser G, Bukowska MA, Briand C, Grütter MG (2009) Crystal structure of the multidrug exporter MexB from *Pseudomonas aeruginosa*. *J Mol Biol* 389:134–145.
7. Koronakis V, Sharff A, Koronakis E, Luisi B, Hughes C (2000) Crystal structure of the bacterial membrane protein TolC central to multidrug efflux and protein export. *Nature* 405:914–919.
8. Akama H, et al. (2004) Crystal structure of the drug discharge outer membrane protein, OprM, of *Pseudomonas aeruginosa*: Dual modes of membrane anchoring and occluded cavity end. *J Biol Chem* 279:52816–52819.
9. Higgins MK, Bokma E, Koronakis E, Hughes C, Koronakis V (2004) Structure of the periplasmic component of a bacterial drug efflux pump. *Proc Natl Acad Sci USA* 101: 9994–9999.
10. Akama H, et al. (2004) Crystal structure of the membrane fusion protein, MexA, of the multidrug transporter in *Pseudomonas aeruginosa*. *J Biol Chem* 279:25939–25942.
11. Symmons MF, Bokma E, Koronakis E, Hughes C, Koronakis V (2009) The assembled structure of a complete tripartite bacterial multidrug efflux pump. *Proc Natl Acad Sci USA* 106:7173–7178.
12. Mikolosko J, Bobyk K, Zgurskaya HI, Ghosh P (2006) Conformational flexibility in the multidrug efflux system protein AcrA. *Structure* 14:577–587.
13. Su CC, et al. (2009) Crystal structure of the membrane fusion protein CusB from *Escherichia coli*. *J Mol Biol* 393:342–355.
14. Bagai I, Liu W, Rensing C, Blackburn NJ, McEvoy MM (2007) Substrate-linked conformational change in the periplasmic component of a Cu(I)/Ag(I) efflux system. *J Biol Chem* 282:35695–35702.
15. Balakrishnan L, Hughes C, Koronakis V (2001) Substrate-triggered recruitment of the TolC channel-tunnel during type I export of hemolysin by *Escherichia coli*. *J Mol Biol* 313:501–510.
16. Borges-Walmsley MI, et al. (2003) Identification of oligomerization and drug-binding domains of the membrane fusion protein EmrA. *J Biol Chem* 278:12903–12912.
17. Aires JR, Nikaido H (2005) Aminoglycosides are captured from both periplasm and cytoplasm by the AcrD multidrug efflux transporter of *Escherichia coli*. *J Bacteriol* 187: 1923–1929.
18. Zgurskaya HI, Nikaido H (1999) Bypassing the periplasm: Reconstitution of the AcrAB multidrug efflux pump of *Escherichia coli*. *Proc Natl Acad Sci USA* 96:7190–7195.
19. Lobedanz S, et al. (2007) A periplasmic coiled-coil interface underlying TolC recruitment and the assembly of bacterial drug efflux pumps. *Proc Natl Acad Sci USA* 104:4612–4617.
20. Harley KT, Djordjevic GM, Tseng TT, Saier MH (2000) Membrane-fusion protein homologues in Gram-positive bacteria. *Mol Microbiol* 36:516–517.
21. Zgurskaya HI, Yamada Y, Tikhonova EB, Ge Q, Krishnamoorthy G (2009) Structural and functional diversity of bacterial membrane fusion proteins. *Biochim Biophys Acta* 1794:794–807.
22. Mergeay M, et al. (2003) *Ralstonia metallidurans*, a bacterium specifically adapted to toxic metals: Towards a catalogue of metal-responsive genes. *FEMS Microbiol Rev* 27: 385–410.
23. Loo JA (1997) Studying noncovalent protein complexes by electrospray ionization mass spectrometry. *Mass Spectrom Rev* 16:1–23.
24. Frottin F, et al. (2006) The proteomics of N-terminal methionine cleavage. *Mol Cell Proteomics* 5:2336–2349.
25. Daniel JM, Friess SD, Rajagopalan S, Wendt S, Zenobi R (2002) Quantitative determination of noncovalent binding interactions using soft ionization mass spectrometry. *Int J Mass Spectrom* 216:1–27.
26. Bligh SW, Haley T, Lowe PN (2003) Measurement of dissociation constants of inhibitors binding to Src SH2 domain protein by non-covalent electrospray ionization mass spectrometry. *J Mol Recognit* 16:139–148.
27. Tjernberg A, et al. (2004) Determination of dissociation constants for protein-ligand complexes by electrospray ionization mass spectrometry. *Anal Chem* 76:4325–4331.
28. Mathur S, Badertscher M, Scott M, Zenobi R (2007) Critical evaluation of mass spectrometric measurement of dissociation constants: Accuracy and cross-validation against surface plasmon resonance and circular dichroism for the calmodulin-melittin system. *Phys Chem Chem Phys* 9:6187–6198.
29. Yum S, et al. (2009) Crystal structure of the periplasmic component of a tripartite macrolide-specific efflux pump. *J Mol Biol* 387:1286–1297.
30. Cherezov V, et al. (2008) Insights into the mode of action of a putative zinc transporter CzrB in *Thermus thermophilus*. *Structure* 16:1378–1388.
31. Goormaghtigh E, Ruysschaert JM, Raussens V (2006) Evaluation of the information content in infrared spectra for protein secondary structure determination. *Biophys J* 90:2946–2957.
32. Auld DS (2001) Zinc coordination sphere in biochemical zinc sites. *Biometals* 14: 271–313.
33. Scherer J, Nies DH (2009) CzcP is a novel efflux system contributing to transition metal resistance in *Cupriavidus metallidurans* CH34. *Mol Microbiol* 73:601–621.
34. Tal N, Schuldiner S (2009) A coordinated network of transporters with overlapping specificities provides a robust survival strategy. *Proc Natl Acad Sci USA* 106:9051–9056.
35. Monchy S, et al. (2007) Plasmids pMOL28 and pMOL30 of *Cupriavidus metallidurans* are specialized in the maximal viable response to heavy metals. *J Bacteriol* 189:7417–7425.
36. Otwinowski Z, Minor W (1997) Processing of X-ray diffraction data collected in oscillation mode. *Methods Enzymol* 276:307–326.
37. Adams PD, et al. (2002) PHENIX: Building new software for automated crystallographic structure determination. *Acta Crystallogr D Biol Crystallogr* 58:1948–1954.
38. Emsley P, Cowtan K (2004) Coot: Model-building tools for molecular graphics. *Acta Crystallogr D Biol Crystallogr* 60:2126–2132.
39. Murshudov GN, Vagin AA, Dodson EJ (1997) Refinement of macromolecular structures by the maximum-likelihood method. *Acta Crystallogr D Biol Crystallogr* 53:240–255.
40. Delano WL (2004) Use of PyMOL as a communications tool for molecular science. *Abstr Pap Am Chem Soc* 228:U313–U314.
41. Emanuelsson O, Brunak S, von Heijne G, Nielsen H (2007) Locating proteins in the cell using TargetP, SignalP and related tools. *Nat Protoc* 2:953–971.
42. Larkin MA, et al. (2007) Clustal W and Clustal X version 2.0. *Bioinformatics* 23: 2947–2948.